ACS OMEGA

http://pubs.acs.org/journal/acsodf

Article

Construction of α-Fe_2O_3/Sulfur-Doped Polyimide Direct Z-Scheme Photocatalyst with Enhanced Solar Light Photocatalytic Activity

Chenghai Ma,* Mingyu Jiang, Changqing Yang, Zuan Yang, Wei Meng, Lian Zhou, Chunyan Sun, and Wanqin Chen

Cite This: *ACS Omega* 2022, 7, 11371−11381

Read Online

ACCESS | Metrics & More | Article Recommendations | Supporting Information

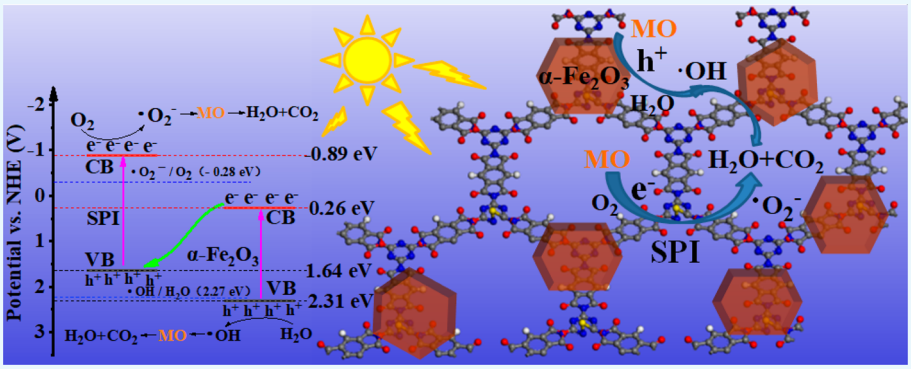

ABSTRACT: A novel two-dimensional α-Fe_2O_3/sulfur-doped polyimide (FO/SPI) direct Z-scheme photocatalyst was successfully constructed by a facile thermal treatment method. The effects of α-Fe_2O_3 nanosheets on the morphology, chemical structure, and photoelectronic properties of FO/SPI composites were systematically characterized by different spectroscopic means. These methods include X-ray diffraction, scanning electron microscopy, X-ray photoelectron spectroscopy, transient fluorescence spectra, and so forth. It was confirmed that the small amounts of α-Fe_2O_3 can availably facilitate exfoliation of bulk SPI, resulting in a transformation of SPI from bulk to 2D layered composite that illustrates tight interface through the coordination Fe−N bond and an all-solid-state direct Z-scheme junction. Thus, the transfer and separation efficiency of photogenerated electron/hole pairs were significantly enhanced, which greatly promoted improvement of the photocatalytic activity of the FO/SPI composite for methyl orange degradation under solar light. This work provides a new approach to constructing efficient inorganic−organic Z-scheme photocatalyst based on strong interface interaction.

1. INTRODUCTION

The photocatalytic degradation of organic pollutants is the focus of environmental science. It can utilize renewable solar energy to clean serious environmental pollution. The key step of the photocatalytic technology is to develop high efficiency photocatalytic materials. The conjugation polymer-based semiconductors have drawn considerable attention for their low cost, abundant sources, unique chemical stability, and good photocatalytic activity.[1−4] As an outstanding representative of conjugated polymer-based photocatalysts, the graphitic carbon nitride ($g\text{-}C_3N_4$) has been used in photocatalytic degradation of organic pollutants, water splitting, and reduction of CO_2 under visible light irradiation.[5−8] Polyimide (PI) as a special polymer semiconductor, represents another kind of the conjugated polymer photocatalyst that can show excellent visible light response for its chemical stability and suitable band structure.[9] However, the photocatalytic activity of PI on degradation of organic pollutants is still low for the inherent feature of the photonic excitation and carrier transport of conjugated polymer.[10] Therefore, a series of strategies including heterojunctions,[11−14] cocatalysts loading,[15−17] and heteroatoms doping[11,18] have been used to improve the photocatalytic efficiency of PI.

In general, the photocatalytic activity can be improved by reducing the dimensions of the photocatalyst to short diffusion length of photogenerated carriers.[19−22] Moreover, constructing Z-scheme photocatalytic materials can efficiently increase solar-light absorption, separation efficiency of the photogenerated electron−hole pairs, and the redox capacity of the photocatalyst, resulting in a significant improvement of the photocatalytic efficiency.[23−27] Despite the enhanced visible

Received: January 24, 2022
Accepted: March 8, 2022
Published: March 22, 2022

light absorption of sulfur-doped polyimide (SPI) after sulfur doping,[18] its photocatalytic activity remains low due to the fast recombination of photogenerated electron−hole pairs. To promote charge separation and transfer, it is particularly important to construct full-solid-state direct Z-mode composite photocatalytic materials combined with another semiconductor material. Similar to SPI, α-Fe_2O_3 is also a potential visible-light-driven photocatalyst due to its intrinsic low cost, nontoxic, thermal stability, environmentally friendly, and corrosion-resistant features.[28] Moreover, α-Fe_2O_3 is an n-type semiconductor with a narrow band gap (about 2.1 eV) and deep valence band (VB). Meanwhile, SPI is also an n-type semiconductor with the higher conduction band bottom level in comparison with α-Fe_2O_3. Therefore, construction of α-Fe_2O_3/SPI composite can effectively enhance its charge separation as well as maintain strong redox activity. On the basis of these considerations, we for the first time constructed a novel 2D α-Fe_2O_3/sulfur-doped polyimide (FO/SPI) Z-scheme photocatalyst for the degradation of methyl orange (MO) through solar-light driven. During the preparation of FO/SPI composites, α-Fe_2O_3 as a catalyst promotes the oxidation stripping of bulk SPI to form 2D layered FO/SPI composites similar to g-C_3N_4, which were confirmed by XRD and SEM. The PL spectral of FO/SPI samples illustrated that the small amount of α-Fe_2O_3 nanosheets can obviously suppress the recombination of photogenerated electron−hole pairs because of their Z-scheme band structure. The effects of α-Fe_2O_3 nanosheets on the solar-light photocatalytic degradation efficiency of FO/SPI composites were systematically investigated. The possible photocatalytic mechanism was also proposed.

2. EXPERIMENTAL SECTION

2.1. Catalyst Preparation. Melamine (MA) and pyromellitic dianhydride (PMDA) were bought from Shanghai Macklin Biochemical Co., Ltd., whereas iron trichloride ($FeCl_3$), sublimed sulfur (S_4), propanetriol ($C_3H_8O_3$), and urea (CH_4N_2O) were purchased from Tianjin Dengke Chemical Reagent Co., Ltd. Triethanolamine (TEOA), KI, $C_4H_{10}O$ (TBA), as well as thiamethoxam (TM) were procured from Sigma-Aldrich. All chemical reagents were used without further purification.

Sulfur-doped polyimide (SPI) was synthesized through a solid−phase thermal polymerization method as previously reported.[18] In a typical procedure, the mixture of 1.26 g of MA, 2.18 g of PMDA, and 25 w.t% of sublimed sulfur (S_4) was put into a semiclosed porcelain crucible and heated to 325 °C with a heating rate of 7 °C min^{-1} using through-nitrogen gas. After keeping this temperature for 4 h under N_2 flow, the resulting solid was cooled to room temperature and milled into powders.

α-Fe_2O_3 was synthesized through a modified method based on previous literature.[29,30] Typically, the mixture of 4.87 g of $FeCl_3{\cdot}6H_20$ and 4.32 g of CH_4N_2O was dispersed in glycerol (10 mL) and deionized water (60 mL) under magnetic stirring. Next, the stirred solution was transferred to a Teflon-lined stainless steel autoclave with an 80 mL capacity and maintained at 180 °C for 12 h. After cooling to room temperature, the obtained mixture was separated by centrifugation and washed with deionized water several times. Then, it was dried at 80 °C for 12 h and further heated to 550 °C for 2 h in an air atmosphere. The obtained gray-black powdered solid was α-Fe_2O_3 after grinding.

The α-Fe_2O_3/sulfur-doped polyimide composites were fabricated by a method similar to that of SPI. The preparation of 5%α-Fe_2O_3/SPI was taken as an example. The mixture of 0.95 g of SPI and 0.05 g of α-Fe_2O_3 was put in a porcelain boat and heated to 325 °C for 4 h before cooling to room temperature. The obtained solid was milled and named as 5%α-Fe_2O_3/SPI and abbreviated as 5FO/SPI. Therefore, the composites of 10%α-Fe_2O_3/SPI, 12%α-Fe_2O_3/SPI, 17%α-Fe_2O_3/SPI, 20%α-Fe_2O_3/SPI, and 28%α-Fe_2O_3/SPI with different contents of α-Fe_2O_3 were prepared and abbreviated as 10FO/SPI, 12FO/SPI, 17FO/SPI, 20FO/SPI, and 28FO/SPI, respectively. The amounts of the reactants for synthesis of the FO/SPI composite samples are summarized in Table S1 of the Supporting Information.

2.2. Characterization. Powder X-ray diffraction (PXRD) measurements of the samples were performed on a Rigaku diffractometer using Cu Kα radiations, and the X-ray tube was operated at 40 kV and 40 mA. FTIR measurements were obtained by using a Nicolet 6700 spectrometer using the KBr pellet support. The scanning electron microscope (SEM) image was recorded on a JSM-6610 system. The transmission electron microscope (TEM), high-resolution transmission electron microscope (HRTEM) was collected with a JEM-2100 electron microscope. Brunner-Emmet-Teller's (BET) method and Barrett−Joyner−Halenda's (BJH) method was taken into consideration to inspect the curves of the surface area and pore size distribution, respectively. UV−vis diffuse reflection spectroscopy (DRS) was taken on a Shimadzu UV−2600 spectrometer using $BaSO_4$ as the reference at room temperature. The photoluminescence (PL) spectrum was performed by an Agilent MY15170004 spectrometer with an excitation wavelength of 350 nm. X-ray photoelectron spectroscopy (XPS) and valence band X-ray photoelectron spectroscopy (VBXPS) were conducted on a PHI 5000 Versa Probe X-ray photoelectron spectrometer with monochromatized Al Ka X-ray radiation. Electron paramagnetic resonance (EPR) measurement was tested by a Bruker EMX-10/12 EPR spectrometer at room temperature. The transient fluorescence spectra of the photocatalysts were recorded by an FLS980 multifunction steady-state and transient fluorescence spectrometer (Edinburgh Instruments) at room temperature.

2.3. Electrochemical Measurements. The photoelectrochemical properties are measured on the traditional three-electrode system. It was made up of the working electrode (the glass with sample), the counter electrode (a Pt sheet), a reference electrode (an Ag/AgCl electrode), and the electrolyte solution (Na_2SO_4, 0.5 mol L^{-1}, pH = 6.8). The working electrode was prepared on fluorine-doped tin oxide (FTO) transparent conductive film glass by electrophoretic deposition method. Typically, the mixture of 50 mg of powder sample and 12 mg of I_2 was dispersed in 45 mL of acetone under sonication for 25 min to obtain the turbid liquid. Meanwhile, two pieces of the FTO transparent conductive film glass that have been arranged on the electrophoretic deposition apparatus were immersed in the turbid liquid, turning on the switch and keeping the voltage at 21 V for 6 min. One piece of the glass with the certain of sample on the conductive face was obtained and dried naturally in air. In order to reduce the influence of the thickness of sample layer and the size of the light irradiation area, the light irradiated on the back side (FTO substrate/semiconductor interface) and the exposure area of each working electrode was 0.28 cm^2. The electrochemical experiments were performed on an electrochemical

https://doi.org/10.1021/acsomega.2c00476
ACS Omega 2022, 7, 11371−11381

analyzer (CHI-663C, Shanghai Chenhua, China). Mott–Schottky curves were taken under dark conditions at 1.0 kHz frequencies. For Nyquist plots measurements, the frequency ranged from 200 kHz to 10 mHz, and the perturbation signal was10 mV.

2.4. Photocatalytic Performance Tests. The photocatalytic activity of the samples was evaluated by the degradation of MO under full arc light irradiation. MO (99.7% purity) was purchased from Tianjin Kemeio Chemical Reagent Co., Ltd. The experimental device for photocatalytic degradation consists of photocatalytic glass reactor, xenon lamp, cryotemperature tank, and magnetic mixer. Light source was achieved by a 300 W xenon lamp (I = 20 A) and a cooling fan. A photocatalytic reactor was a Pyrex top-irradiation full glass container with a constant temperature water system for holding temperature at 25 °C. In each test, 0.2 g of catalyst was dispersed in 100 mL aqueous solution of MO (4 mg L^{-1}), and the suspension was magnetically stirred in the dark for 1 h to reach the adsorption–desorption equilibrium before light irradiation. At predetermined time intervals, 4 mL of suspension was collected and centrifuged to remove most of the catalyst particles. Then the obtained clear solution was filtered through MCE 0.45 μm and analyzed by measuring its absorbance with an UV–vis spectrometer (Mepoda UV-1800) at 464 nm. Using the same method, the photocatalytic degradation activitives of the TM as a colorless pollutant besides the dye were tested. The only difference is that the measured absorption wavelength was at 310 nm.

2.5. Recyclability of FO/SPI Composites. To further evaluate the cyclic stability of photocatalytic materials, experiments were conducted for 6 runs, and the irradiation time of each run was 180 min. The used photocatalyst could be conveniently filtered and collected from the solution by centrifugation and added back into the reactor for the next run.

3. RESULTS AND DISCUSSION

3.1. Structure and Morphology Analysis. The XRD patterns of pristine SPI, α-Fe_2O_3, and FO/SPI composites with different α-Fe_2O_3 contents were illustrated in Figure 1. Several distinct peaks in the range of 10–30° appeared on the pattern of pristine SPI, which is consistent with the XRD diffraction peaks of SPI reported in the previous literature.[18] Meanwhile, the XRD characteristic peaks of α-Fe_2O_3 (JCPDF: 52–1449) can be obviously observed in the FO/SPI composites. The intensities of two peaks (102) at 33.1° and (110) at 37.2° and other peaks attributed to α-Fe_2O_3 gradually increasing for increased loadings of α-Fe_2O_3 in the composites, confirming that the α-Fe_2O_3 was indeed introduced into the SPI. Amazingly, most of the XRD characteristic peaks of SPI disappeared after combining with α-Fe_2O_3 nanosheets. This may be because the SPI was oxidized and stripped to form a 2D-layered material by α-Fe_2O_3 as a catalyst[31] during the synthesis of the FO/SPI composite. The weak characteristic peak located at ~13° in the XRD spectrum of the conjugated polymer is attributed to an in-plane repeat period of 0.861 nm in the crystal.[1] It has vanished after introducing α-Fe_2O_3 into the SPI to form FO/SPI hybrids, presumably because of the

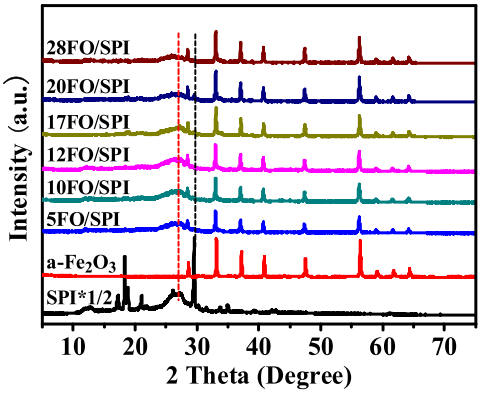

Figure 1. XRD patterns of pristine SPI, α-Fe_2O_3, and FO/SPI composites with different α-Fe_2O_3 contents.

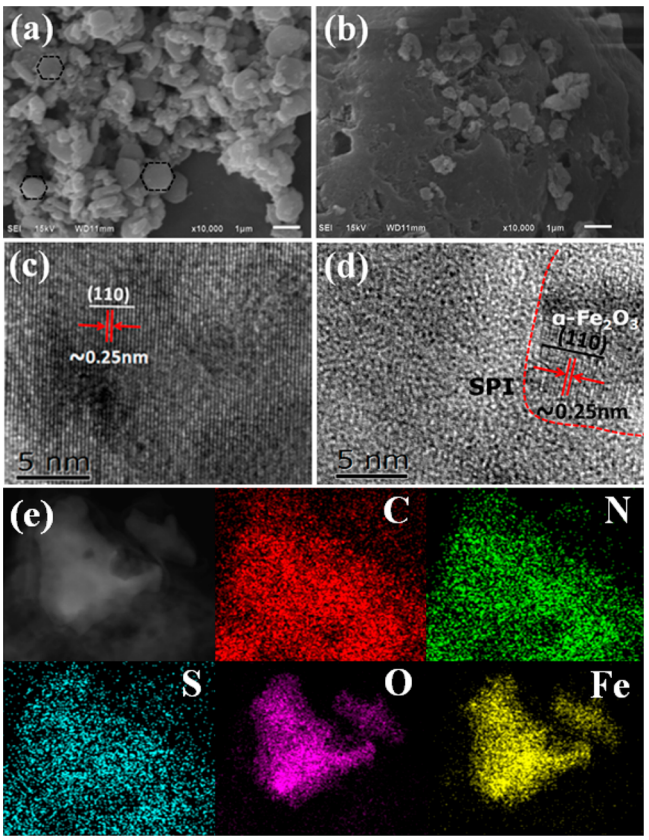

Figure 2. Images of SEM (a,b) and TEM (c,d) for α-Fe_2O_3 and 17FO/SPI composite, and EDX elemental mappings of C, N, S, O, and Fe for the 17FO/SPI composite (e).

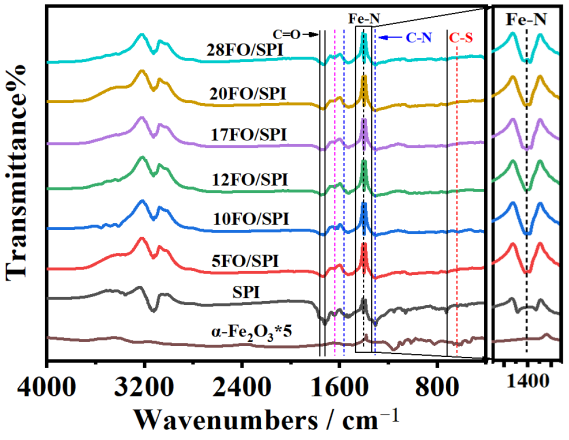

Figure 3. FT-IR spectra of α-Fe_2O_3, SPI, and FO/SPI composites.

https://doi.org/10.1021/acsomega.2c00476
ACS Omega 2022, 7, 11371–11381

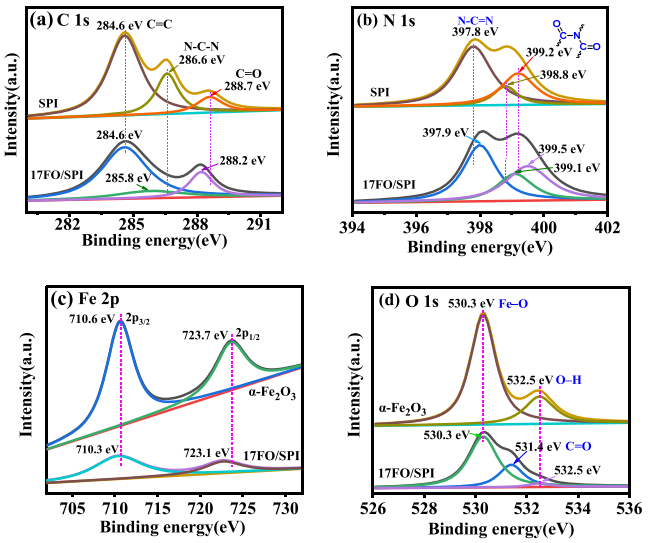

Figure 4. XPS spectra for (a) C 1s, (b) N 1s, (c) Fe 2p, and (d) O 1s of SPI, α-Fe_2O_3, and 17FO/SPI composite.

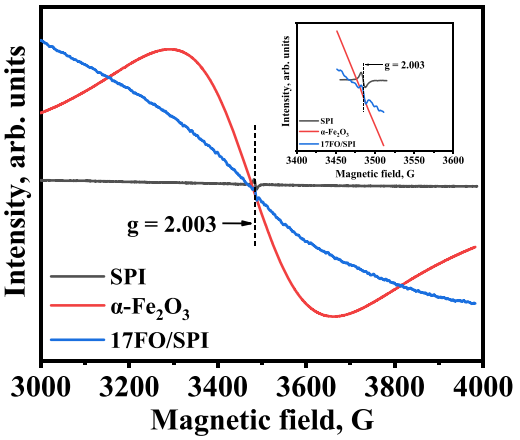

Figure 5. EPR spectra of SPI, α-Fe_2O_3, and 17FO/SPI composite samples at room temperature.

strong interaction between α-Fe_2O_3 and SPI, thus affecting the formation of an in-plane repeat period in the preparation of FO/SPI hybrid photocatalysts. Moreover, the strong distinct peak centered about ~18° and ~29.7°, respectively, representing the polymerization degree of the SPI[16] have disappeared, but the characteristic peak at ~27.4° reflecting the stacking of π-conjugated two-dimensional (2D) frameworks of SPI still exist in the XRD patterns of FO/SPI composites. These may be attributed to the special thermal preparation process of FO/SPI composites. In detail, the SPI first was oxidized and stripped under the catalysis of α-Fe_2O_3 to form some oligomeric polyimides,[31] and then these oligomers further repolymerized with the aid of the π–π electronic interaction or hydrogen bonding between the conjugated core units, resulting in an assembly of highly regular and symmetrical polymer frameworks.[18] Thus, the more orderly layered 2D-FO/SPI hybrids formed through a new preparation method of 2D FO/SPI composites including exfoliation and further repolymerization.

To further determine the morphology of the prepared samples and the existence form of α-Fe_2O_3 on SPI, SEM, TEM, and EDS measurements were carried out. As shown in Figure 2a, most of α-Fe_2O_3 nanosheets crystals displayed

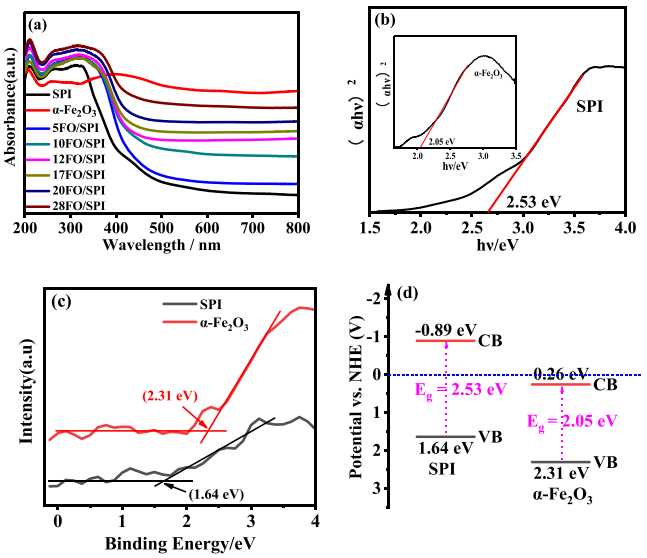

Figure 6. (a) UV–vis DRS spectra of as-prepared pure SPI, α-Fe_2O_3, and 17FO/SPI composites. (b) The corresponding plots of $(\alpha h \nu)^2$ versus $h \nu$, (c) VBXPS spectra, and (d) schematic illustration of band structures for SPI and α-Fe_2O_3.

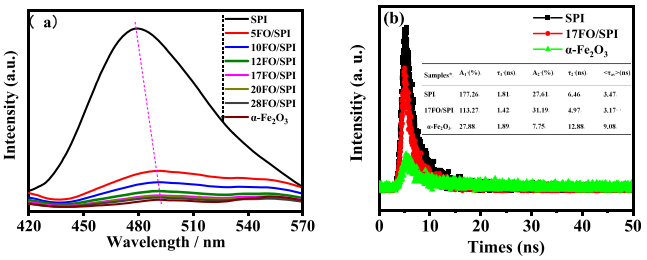

Figure 7. (a) Comparison of photoluminescence (PL) spectra of SPI, FO/SPI composites, and α-Fe_2O_3 samples. (b) Transient PL decay spectra for pure SPI, 17FO/SPI and α-Fe_2O_3.

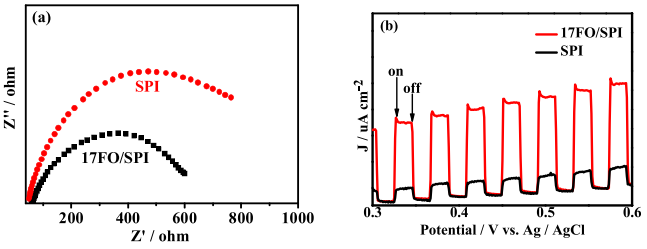

Figure 8. (a) EIS Nyquist plots of electrochemical impedance spectroscopy with SPI and 17FO/SPI composite in the dark. (b) Photocurrent–potential curves of SPI and 17FO/SPI electrode in the 0.5 mol L^{-1} Na_2SO_4 aqueous solution under full arc light irradiation.

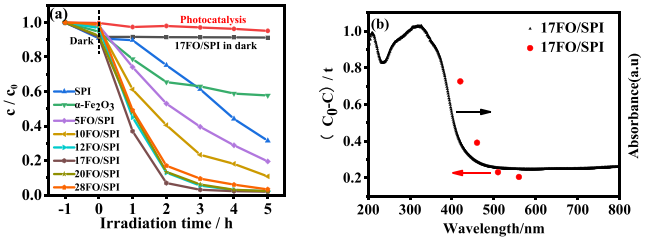

Figure 9. (a) Comparison of the photocatalytic degradation of MO over different catalysts under full arc light (λ > 300 nm). (b) Dependence of degradation activity on wavelength by 17FO/SPI.

https://doi.org/10.1021/acsomega.2c00476
ACS Omega 2022, 7, 11371–11381

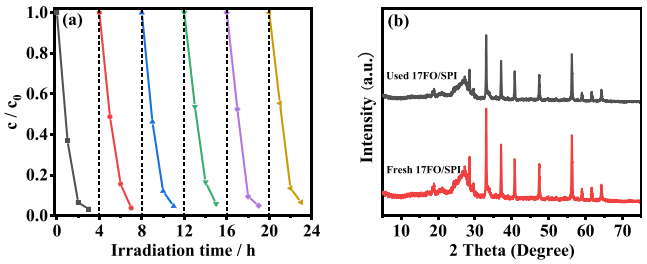

Figure 10. (a) Cycling runs for the photodegradation of MO in the presence of the 17FO/SPI composite sample under full arc light illumination. (b) XRD patterns of the 17FO/SPI before and after photocatalytic degradation of MO under full arc light illumination.

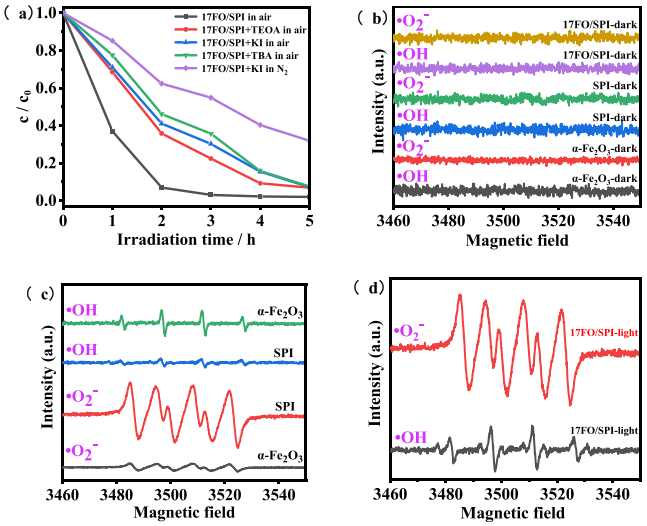

Figure 11. (a) The effects of TEOA, KI, TBA, and purging-N_2 as h^+, ·OH, and $\cdot O_2^-$ sacrificial agents on the photocatalytic degradation of MO in the presence of the 17FO/SPI composite under full arc light irradiation. (b) DMPO spin-trapping ESR spectra of α-Fe_2O_3, SPI, and 17FO/SPI composite without light irradiation. (c,d) DMPO spin-trapping ESR spectra of α-Fe_2O_3, SPI, and 17FO/SPI composite (in aqueous for DMPO-·OH; in methanol for DMPO-$\cdot O_2^-$).

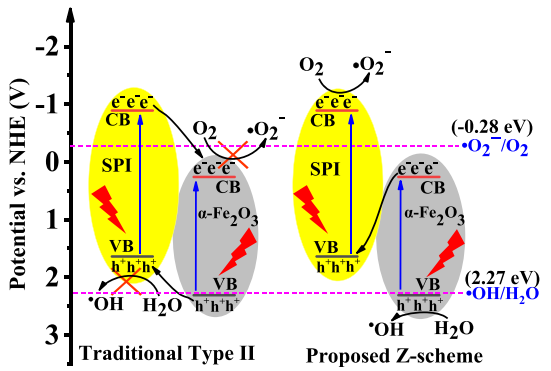

Figure 12. Schematic illustration of the traditional type-II heterojunction and the proposed Z-scheme charge transfer mechanism.

uniform hexagonal morphology with the thickness of ~50 nm. HR-TEM images obviously demonstrate a lattice spacing of ~0.25 nm, which matches well with the (110) plane of α-Fe_2O_3 crystals (Figure 2c). The SPI sample presents porous and rough bulk morphology (Figure S1). But the layered morphology of the 17FO/SPI composite sample can be clearly observed, indicating the transformation of SPI from bulk to 2D layers of FO/SPI composite as shown in Figure 2b. Meanwhile, the junctions of α-Fe_2O_3 nanosheets crystals/2D layers SPI composite were successfully constructed, which was evidenced by the observation of sharp interfaces between α-Fe_2O_3 nanosheets and 2D layers SPI in 17FO/SPI sample with α-Fe_2O_3 loading (Figure 2d). The energy dispersive X-ray (EDX) elemental mapping of the 17FO/SPI composites on a microscope further suggests uniform distribution of α-Fe_2O_3 over 2D SPI surface (Figure 2e and Figure S2). In addition, the BET-specific surface area and BJH pore size distributions of the as-prepared samples were assessed by the N_2 adsorption−desorption test. Obviously, each sample exhibited a type IV with a H3 hysteresis loop, illustrating the presence of a mesoporous structure within the samples (Figure S3). The pore size distributions of all samples were predicted by the BJH method (Figure S3b of the Supporting Information). The average pore diameter, specific surface area, and pore volume of all samples were measured by the BET method (Table S2). Pure α-Fe_2O_3 has a low surface area but the SPI and FO/SPI composites have appropriate surface area for efficient absorption as well as degradation. Thus, the SPI acts as the support for α-Fe_2O_3 to enhance its surface area.

The interface interaction of FO/SPI is verified by FTIR spectroscopy (Figure 3). As shown in the FTIR spectrum, all of the FO/SPI composite samples exhibit the characteristic absorption bands of sulfur-doped polyimide.[18] The bands at 1787.5, 1723.5, and 726.3 cm^{-1} are ascribed to the asymmetric stretching, symmetric stretching, and bending vibrations of the −C═O bond in the PMDA moiety of SPI, respectively. The bands at 1553 and 1308 cm^{-1} marked with blue dotted lines are indicative of the stretching vibration of C−N−C in the five-membered imide rings and breathing modes of aromatic C═N in the triazine unit, respectively.[32] The weak characteristic vibrating peak of the S−N bond at 632 cm^{-1} marked with a red dotted line[33] was also observed in a series of samples. These results indicate that the main bonding skeleton or chemical framework of SPI has not been changed after introducing the Fe species into SPI. However, the broad peaks at around 3100−3400 cm^{-1} assigned to the typical amine groups, hydrogen bonds, and water molecule were observed that it became weak after loading α-Fe_2O_3 on SPI.[33] It may have attributed to the partial stripping of layered structure of SPI during the solid phase thermal synthesis of FO/SPI composites, because of the multiple O−H bond interactions of interlayer and absorbed H_2O were lost at 352 °C, which matches well with XRD results. Meanwhile, the infrared characteristic absorption peaks of α-Fe_2O_3 were not observed in a series of FO/SPI samples and may be attributed to the very weak absorption strength of iron oxide and its high dispersion on the SPI surface. In addition, it is surprising that a new peak at 1403 cm^{-1} appeared in the spectra of all FO/SPI composites, which is assigned to the characteristic peaks of the Fe−N bond.[34] The formation of the Fe−N bond is likely to arise from coordination of the N atoms of heptazine units to the unsaturated Fe sites of α-Fe_2O_3 in the interface of FO/SPI. This Fe−N bond confirmed that there is a strong chemical interaction between α-Fe_2O_3 and SPI, thus leading to construct an intimate contact interface. The intimate contact interface between α-Fe_2O_3 and SPI can promote the transfer of the photogenerated carriers.

To further pursue the surface chemical state of the elements in the involved samples, XPS spectra of the as-prepared SPI, α-

https://doi.org/10.1021/acsomega.2c00476
ACS Omega 2022, 7, 11371−11381

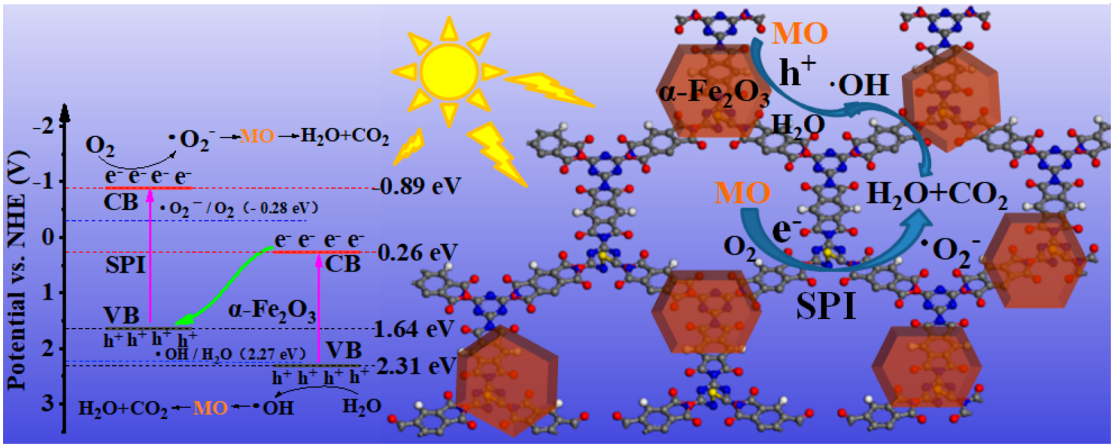

Figure 13. Schematic of the photogenerated charge carrier's separation and transfer in the FO/SPI system under full arc light irradiation.

Fe_2O_3 and 17FO/SPI composite were recorded at room temperature. The binding energies of the elements were calibrated by the C 1s peak (284.6 eV), arising from adventitious carbon. The corresponding high resolution XPS spectra of C 1s, N 1s,

Fe 2p and O 1s of the photocatalysts are shown in Figure 4, respectively. The C 1s XPS spectra of SPI are obviously observed from Figure 4a. In three C 1s peaks located at 284.6, 286.6, and 288.7 eV, the C 1s peak at 284.6 eV was ascribed to the sp^2 C═C bonds or adventitious carbon, while the peaks centered at 286.6 and 288.7 eV could be attributed to the N−C−N bond and the C═O in the triazine rings of SPI, respectively. For the N 1s XPS spectra of SPI and 17FO/SPI composite, it could be shown in Figure 4b. The N 1s peak at ∼397.8 eV corresponds to the sp^2−bonded N in the triazine rings (N−C═N) of SPI. At the same time, a pairs of peaks at the binding energies of 398.8 and 399.2 eV are stemmed from the splitting of the peak of nitrogen atoms in the five-membered imide ring of polyimide (PI) after incorporating sulfur into the triazine ring of PI. These results are matched well with the previous literature values.[17] By more carefully comparing the spectrum of 17FO/SPI composite with that of the pristine SPI, it can be clearly observed that the binding energies of N 1s for the 17FO/SPI at 397.9, 399.1, and 399.5 eV shifted toward high binding energies. In addition, the binding energies of Fe 2p for α-Fe_2O_3 are determined to be 710.6 and 723.7 eV as shown in Figure 4c, which matched well with reported values of the Fe $2p_{3/2}$ and Fe $2p_{1/2}$, ascribing to 3+ oxidation states of iron.[35] Obviously, the binding energies of Fe 2p for the 17FO/SPI composite at 710.3 and 723.1 eV corresponding to the Fe $2p_{3/2}$ and Fe $2p_{1/2}$ shifted toward lower binding energies compared to that of pure α-Fe_2O_3. As previously reported, the sp^3-hybridized N atoms in tertiary nitrogen groups of g-C_3N_4 can provide the lone pair electrons to the unoccupied d orbital of metal atoms to form M (δ^+)−N (δ^-) bonding states through chemical coupling interaction.[36] Intriguingly, the similar interaction also exits in our FO/SPI composite. The lone pair electrons of N atoms in the integral conjugated framework of SPI interact with the unoccupied d orbital of Fe atoms in α-Fe_2O_3, leading to the increase of N 1s binding energy and the reduction of Fe 2p binding energy in 17FO/SPI composite compared that of pristine SPI and α-Fe_2O_3. Thus, the interaction between α-Fe_2O_3 nanosheets and SPI is consistent with the formation of Fe−N bond in the infrared spectrum of the 17FO/SPI composite sample. However, the binding energy of O 1s in the high-resolution O 1s XPS spectra did not obviously changed as shown in Figure 4d. The peak at 530.3 eV is attributed to lattice oxygen in α-Fe_2O_3, and the peak at 532.5 eV is assigned to surface −OH groups/adsorbed water.[37] Besides these two peaks, a new O 1s peak centered at 531.4 eV was observed in the XPS spectrum of the 17 FO/SPI composite, which is assigned to the C═O in the five-membered imide ring of SPI.[38] For the unchanged binding energies of O 1s after introducing α-Fe_2O_3 on SPI, this may be ascribed to the higher electronegativity of an oxygen atom than that of a nitrogen atom. Thus, the stronger chemical interaction between SPI and α-Fe_2O_3 was promoted to form covalent Fe−N bonding states. The formation of Fe−N bonding states benefits the transport and separation of photogenerated carriers between polymer supports and transition metal oxide leading to a great improvement in photocatalytic activity and stability of inorganic−organic composite semiconductor materials. In addition, the electron paramagnetic resonance (EPR) was conducted to further reveal the interaction between α-Fe_2O_3 and SPI at room temperature. From Figure 5, it can be observed that the Lorentzian line centered at a g value (2.003) is detected on the spectra of SPI and 17 FO/SPI composite powder samples in the magnetic field from 3000 to 4000 G. The peak signal at g value equivalent to 2.003 is attributed to an unpaired electron on the carbon atoms of the aromatic rings within π-bonded nanosized clusters.[39] Moreover, the EPR intensity of the peak at g = 2.003 of the 17 FO/SPI composite clearly strengthened more than that of SPI, implying that the extension of the conjugate system sharply enhanced after introducing α-Fe_2O_3 into SPI.

3.2. Optical and Electronic Properties. The optical absorption properties of SPI, FO/SPI, and α-Fe_2O_3 samples were investigated by UV−vis diffuse reflection spectra and converted to Kubelka−Munk function. As shown in Figure 6a, after combining with α-Fe_2O_3 nanosheets the absorption band edge of SPI is obviously red-shifted and the light absorption intensity of FO/SPI samples significantly enhanced with the increasing concentration of α-Fe_2O_3. The bulk SPI possessed an absorption edge at 475 nm and a corresponding band gap of 2.53 eV (Figure 6b), while the absorption edge of 17FO/SPI sample red-shifted to 510 nm, resulting in a band gap of 2.35 eV (Figure S4). This optical property of UV−vis spectra shows the generation of new localized electronic states (surface states) within the band gap of SPI,[40] which may induce the

https://doi.org/10.1021/acsomega.2c00476
ACS Omega 2022, 7, 11371−11381

absorption of visible light. Therefore, the absorption intensities of FO/SPI samples were remarkably enhanced in the range of 400−800 nm. The increased visible light absorption and the decreased band gap of the composites are beneficial to the production of photogenerated electrons and holes, thus promoting the enhancement of their photocatalytic activity. Moreover, the bandgap of the prepared samples can be calculated by the Kubelka−Munk function equation, $\alpha hv = A(hv - E_g)^{1/2}$.[34] From Figure 6b, it can be clearly observed that the band gaps of SPI and α-Fe_2O_3 samples were approximately 2.53 and 2.05 eV, respectively, which obtains from extrapolation of the linear region of the absorbance squared versus energy. Meanwhile, the VBXPS spectra of SPI and α-Fe_2O_3 samples displayed that the energy levels of valence band (VB) in SPI and α-Fe_2O_3 are about 1.64 and 2.31 eV, respectively, as shown in Figure 6c. In addition, combining these findings with the UV−vis and VBXPS results, the conduction band (E_{CB}) potentials are −0.89 and 0.26 eV for SPI and α-Fe_2O_3 versus NHE calculated by the equation $E_{CB} = E_{VB} - E_g$.[41] The conduction band (E_{CB}) potentials can also be estimated by the Motshoky curves. As shown in Figure S5, the flat band potentials (E_{fb}) of SPI and 17FO/SPI are −0.89 and −1.08 V versus Ag/AgCl, respectively. It is well-known that the CB level is generally more negative about −0.1 or −0.2 V than its flat band potential for n-type semiconductor.[34] Thus, the E_{CB} for SPI and 17FO/SPI is presumably −0.89 and −1.08 V, respectively. Therefore, the CB level of SPI changed significantly after binding to α-Fe_2O_3. So the schematic band structure of SPI and α-Fe_2O_3 was determined using these results as illustrated in Figure 6d.

To reveal the efficiency of charge carrier trapping, transfer, and separation in prepared samples, photoluminescence (PL) measurement was carried out, as shown in Figure 7a. After combining with α-Fe_2O_3 nanosheets, the fluorescence intensities of the FO/SPI composite powder samples sharply decreased compared with that of the SPI powder sample. This result indicates that the construction of Z-scheme FO/SPI efficiently suppressed the radiative recombination of the photogenerated electrons and holes, which is mainly attributed to the excellent charge carriers transport principle of Z-scheme FO/SPI interface structure between α-Fe_2O_3 nanosheets and 2D SPI and reduced dimension of FO/SPI semiconductors. In addition, the time-resolved photoluminescence (TRPL) decay spectra of SPI, 17FO/SPI, and α-Fe_2O_3 samples were exhibited in Figure 7b. The lifetimes about τ_1 and τ_2 of the 17FO/SPI composite are between SPI and α-Fe_2O_3, respectively. It may be caused by the combination of SPI and α-Fe_2O_3. The average lifetime τ_{av} are 3.47, 3.17and 9.08 ns for SPI, 17FO/SPI and α-Fe_2O_3, respectively. The result showed that the lifetime of excited state of the 17FO/SPI composite was shorter than that of SPI and α-Fe_2O_3.[42] Moreover, the decreased lifetime of photoexcited charges was concerned with promoted electron transport.[34]

To further investigate the electrochemical conductivity properties of the prepared samples, EIS as a powerful tool was used. The impedance of the EIS Nyquist plot is the impedance of the copper foil/photocatalyst, photocatalyst/photocatalyst, and photocatalyst/electrolyte interfaces. The lower the impedance is, the lower the interface resistance is and the higher the separation efficiency of the photogenerated carriers is.[43−45] As displayed in Figure 8a, the semidiameter of the Nyquist curve for 17FO/SPI composite was much smaller than that of SPI, showing the FO/SPI composite has better electron transport capability than SPI alone. Meanwhile, the photocurrent response was then performed to further study the charge transfer behavior of the prepared samples.[46] The photocurrent responses of 17FO/SPI and SPI after deposition on FTO electrodes versus Ag/AgCl under full arc light irradiation are shown in Figure 8b. It can be clearly observed that the photocurrent density over 17FO/SPI is significantly enhanced, which is about 5.0 times as high as that of bulk SPI. Ordinarily, the formation of the photocurrent is mainly attributed to the diffusion of the photogenerated electrons to the back contact and simultaneously the photoinduced holes are taken up by the hole acceptor in the electrolyte. Therefore, the enhanced photocurrent of 17FO/SPI sample indicates a longer lifetime of the photoinduced charge carriers and more efficient separation of photogenerated electron/hole pairs than that of bulk SPI sample, which is consistent with PL analysis and beneficial for its improved photocatalytic activity.

3.3. Photocatalytic Activity and Mechanism. The photocatalytic activities of SPI, α-Fe_2O_3 and FO/SPI composite powder samples are examined by the degradation of MO in solution (4 mg L^{-1}). Usually, the initial concentrations of MO are identical for all the samples, while the concentration of MO at the time as the light was turned on did differ (in Figure 9a) because the specific surface area varied for each sample (Table S2). As shown in Figure 9a, the photolysis of MO under full arc light (simulation of solar light) irradiation is negligible in the absence of the photocatalyst. Meanwhile, little degradation of methyl orange was observed on the 17FO/SPI composite sample in dark condition even for 5 h due to the stable structure of MO. However, the prepared samples displayed different degradation activity for MO under the irradiation of a xenon 300 W lamp without a cut-off filter, demonstrating that the degradation of MO was indeed driven by full arc light. The direct correlation between the activity of the 17FO/SPI composite sample and the energy of irradiated light was further confirmed by the wavelength dependence experiment using different pass-filters. From Figure 9b, it can be observed that the degradation activity trend is consistent with its absorption edge, which illustrates that the reaction of photocatalytic degradation is really driven by the bandgap transition of the 17FO/SPI composite sample. Obviously, the photocatalytic activities of all FO/SPI composites are higher than those of pristine SPI and α-Fe_2O_3, indicating the close binding of α-Fe_2O_3 and SPI not only extends absorption for visible light but also promotes the separation of photogenerated electrons and holes, thus leading to a significant improvement of the photocatalytic activity on SPI sample. Moreover, with the increase of α-Fe_2O_3 content on SPI the photocatalytic degradation activity of FO/SPI composites increases and reached a maximum for the 17FO/SPI composite sample, which is about 3.8 times higher than that of SPI in 2 h. Then, the degradation activity of 20FO/SPI and 28FO/SPI composite samples gradually decreased by increasing the α-Fe_2O_3 content on SPI. As for the drop in the activity of the samples with heavy loadings of α-Fe_2O_3, it is likely due to the insignificant increase of photogenerated electrons and holes separation efficiency compared to that of the 17FO/SPI composite sample. As shown in Figure 7, the PL spectra lines of 17-, 20-, and 28FO/SPI composite samples almost overlap, indicating adding more α-Fe_2O_3 in SPI does not cause an increase in the separation efficiency of photoelectron/hole pairs. In addition, the effect of pH on the photocatalytic activity of catalyst is indeed a key factor in determining the

https://doi.org/10.1021/acsomega.2c00476
ACS Omega 2022, 7, 11371−11381

photocatalytic reaction.[47] We performed a series of experiments to determine the photocatalytic degraded MO activities of the 17FO/SPI composite sample at the distinct pH values like 1, 3, 5, 7, 9, and 11 acquired by the subsequent addition of $NH_3{\cdot}H_2O$ or HCl. As shown in Figure S6a, The photocatalytic degradation methyl orange activity of the 17FO/SPI composite first enhances then decreases with increasing pH values. Obviously, the highest degrading efficiency of 17FO/SPI was determined to be 87.9%, with rate constants of 0.7 h^{-1} at PH = 7 (Figure S6b). To compare the photocatalytic activity of FO/SPI composite with other systems, we prepared g-C_3N_4 according to the literature method,[6] and then prepared the 17 wt %α-Fe_2O_3/g-C_3N_4 (17FO/CN) sample by using a synthetic method of 17FO/SPI sample. It is clearly observed that the photocatalytic degradation MO activity of 17FO/SPI is better than 17FO/CN under the same photocatalytic reaction conditions (Figure S7). In order to avoid color sensitivity, the photocatalytic degradation activities of the TM as a colorless pollutant besides dye were tested. Apparently, the photolysis of TM under full arc light irradiation is negligible in the absence of photocatalyst. However, the prepared the 17FO/SPI sample displayed the good degradation activity for TM under the light irradiation (Figure S8). It is shown that the degradation of TM is indeed a photocatalysis of FO/SPI composite sample but not color sensitivity. To further study the effects of the amount of photocatalyst and the initial concentration of pollutants on the photocatalytic activities, the contrast experiments were carried out. As shown in Figure S9a, the photocatalytic activity of the 17FO/SPI composite increases with the increasing amount of the catalyst. However, the excessive amount of the catalyst did not significantly enhance its photocatalytic activity. In addition, the change in the initial pollutant concentration did not cause significant differences in the photocatalytic activity of 17FO/SPI composite (Figure S9b).

For a good photocatalyst, another important criterion is high durability. To investigate the cyclic stability of a prepared catalyst, photocatalytic degradation of MO was continuously conducted on the 17FO/SPI composite sample for 1080 min in six cycles. As displayed in Figure 10a, it can be clearly observed that there is no obvious abate in the photocatalytic degradation activity of the 17FO/SPI sample after 6 runs. Meanwhile, its powder XRD pattern is similar before and after photocatalytic reaction of MO degradation (Figure 10b). These results demonstrate that the FO/SPI composite sample has satisfactory recyclability and stability for the photocatalytic degradation of organic pollutants.

To further inquire about the photocatalytic degradation MO mechanism of the FO/SPI composite in detail, a series of controlled experiments were conducted in the different reaction conditions. Normally, photogenerated electrons can reduce oxygen to form reactive superoxide radical anion ($\cdot O_2^-$), and photogenerated holes can react with water to produce hydroxyl radicals ($\cdot$OH).[48] Therefore, through incoming nitrogen gas to removal of oxygen experiments were first performed to determine the effect of photogenerated electrons on photocatalytic degradation MO activity of FO/SPI composite. From Figure 11a, it is clearly observed that the photocatalytic activity of 17FO/SPI significantly reduced under N_2, illustrating photogenerated electrons that play a key role. Moreover, since the photogenerated holes can oxidize I^- into I_2, the experiment using KI as a hole sacrificial agent was conducted to determine the effect of holes on photocatalytic activity. Minor decrease of photocatalytic activity on the 17FO/SPI composite sample was observed after the addition of KI (Figure 11a), indicating the photogenerated holes do not play a leading role in photocatalysis. This result was further confirmed by using $C_4H_{10}O$ (TBA) and triethanolamine (TEOA) as $\cdot$OH and h^+ sacrificial agents, respectively (Figure 11a). As is well-known, the $\cdot OH/H_2O$ potential is 2.27 eV,[49] and the $\cdot O_2^-/O_2$ potential is −0.28 eV.[50] From Figure 12, we can see that the valence band position (1.64 eV) (Figure 6d) of SPI is not positive enough to oxidize H_2O into $\cdot$OH (2.27 eV),[51] but it can reduce the absorbed O_2 to form $\cdot O_2^-$ because that the CB level of SPI at −0.89 eV (Figure 6d) is more negative than the $\cdot O_2^-/O_2$ potential (−0.28 eV). Meanwhile, it is also observed that the VB and CB levels of α-Fe_2O_3 are 2.31 and 0.26 eV (Figure 6d), respectively. So the photogenerated holes (h^+) on the valence band of α-Fe_2O_3 can oxidize H_2O to yield $\cdot$OH, and its photogenerated electrons (e^-) cannot react with O_2 to form $\cdot O_2^-$ because its CB level (0.26 eV) is not negative enough to drive the reduce process of O_2 to form $\cdot O_2^-$.[52] These analyses are further confirmed by the ESR spin-trapping using 5,5-dimethyl1-pyrroline N-oxide (DMPO) as a spin trap to stabilize radicals. To detect the transient radical intermediates, ESR was performed in aqueous solution (for DMPO-$\cdot$OH) and methanol solution (for DMPO-$\cdot O_2^-$),[53] respectively. From Figure 11b, it can be observed that no signals of DMPO-$\cdot$OH and DMPO-$\cdot O_2^-$ were detected from α-Fe_2O_3, SPI, and 17FO/SPI hybrid samples without light irradiation.[54] As shown in Figure 11c, the strong signals of DMPO-$\cdot$OH and DMPO-$\cdot O_2^-$ were detected from α-Fe_2O_3 and SPI under light irradiation, respectively. Meanwhile, no obvious signals of $\cdot$OH and $\cdot O_2^-$ were observed in the SPI and α-Fe_2O_3 samples under the same condition, respectively. Significantly, the obvious $\cdot$OH and $\cdot O_2^-$ signals were simultaneously detected in the presence of the 17FO/SPI composite (Figure 11d). Moreover, the strong signals of $\cdot$OH and $\cdot O_2^-$ were also simultaneously detected in the presence of the 5FO/SPI and 28FO/SPI composites under full arc light irradiation (Figure S10). Thus, if it is a traditional type-II heterojunction[55] between α-Fe_2O_3 and SPI (Figure 12), the holes of α-Fe_2O_3 should transfer to the VB of SPI, which cannot oxidize H_2O into $\cdot$OH and will lead to a more serious photocorrosion. Usually, photocorrosion happens due to the sulfide being oxidized by holes. If so, it is unlikely that the FO/SPI composite can have a good photocatalytic stability. At the same time, the photogenerated electrons (e^-) of SPI transfer to the CB of α-Fe_2O_3, which cannot react with O_2 to form $\cdot O_2^-$. Therefore, it should be a direct Z-scheme route[56,57] of photogenerated carriers existing in the FO/SPI composite photocatalyst.

On the basis of the above results, we proposed a Z-scheme photocatalytic mechanism for the enhanced activity and stability of FO/SPI composite as shown in Figure 13. Under full arc light irradiation, both SPI and α-Fe_2O_3 were excited to yield photogenerated electron (e^-)/hole (h^+) pairs. Then the photoexcited e^- in the CB of α-Fe_2O_3 easily recombine with the photoexcited h^+ on the VB of SPI, resulting in numerous more active photogenerated e^- and h^+ remaining in CB of α-Fe_2O_3 and VB of SPI, respectively. The remaining e^- in the CB of SPI can easily be captured by O_2 to form $\cdot O_2^-$ while the h^+ left behind in the VB of α-Fe_2O_3 can react with H_2O to yield $\cdot$OH.[58,59] Both active species $\cdot O_2^-$ and $\cdot$OH can easily oxidize MO to form inorganic small molecules, such as CO_2, H_2O, and

https://doi.org/10.1021/acsomega.2c00476
ACS Omega 2022, 7, 11371−11381

so forth.[60,61] Thus, an effective process of photocatalytic degradation of MO proceeds smoothly.

4. CONCLUSIONS

In summary, we adopt a facile thermal treatment method to successfully construct a novel 2D direct Z-scheme photocatalyst. The small amounts of α-Fe_2O_3 can availably facilitate exfoliation of bulk SPI, resulting in a transformation of SPI from bulk to 2D layered hybrid, which illustrates tight interface and an all-solid-state Z-scheme junction through the coordination Fe−N bond. Thus, the transmission and separation efficiency of photogenerated electron−hole pairs were significantly enhanced, which greatly promoted improvement of the activity and durability of the FO/SPI composite for MO degradation under solar light.

■ ASSOCIATED CONTENT

Supporting Information

The Supporting Information is available free of charge at https://pubs.acs.org/doi/10.1021/acsomega.2c00476.

Amounts of the reactants for synthesis of the FO/SPI samples; image of SEM for bulk SPI sample; images of EDX elemental mappings and the content distribution diagram of N, Fe, S, O, and C for 17FO/SPI composites; N_2 adsorption/desorption isotherms and BJH plot for pore size distribution in as-prepared photocatalysts; corresponding plots of $(\alpha h\nu)^2$ versus $h\nu$ for the 17FO/SPI composite sample; effect of solution pH on the photocatalytic degradation of MO (a) activities and (b) kinetics of 17FO/SPI composite sample; comparison of the photocatalytic degraded MO activity of 17FO/CN and 17FO/SPI samples under full arc light illumination; study of the photocatalytic degradation of TM over time; DMPO spin-trapping ESR spectra of 5FO/SPI and 28FO/SPI composite (in aqueous for DMPO-•OH, in methanol for DMPO-$•O_2^-$) under full arc light irradiation (PDF)

■ AUTHOR INFORMATION

Corresponding Author

Chenghai Ma − *State Key Laboratory of Plateau Ecology and Agriculture, Qinghai University, Xining 810016, China; School of Chemical Engineering, Qinghai University, Xining 810016, China;* orcid.org/0000-0002-4965-3024; Email: chmaqhu@163.com

Authors

Mingyu Jiang − *State Key Laboratory of Plateau Ecology and Agriculture, Qinghai University, Xining 810016, China; School of Chemical Engineering, Qinghai University, Xining 810016, China*

Changqing Yang − *School of Chemical Engineering, Qinghai University, Xining 810016, China*

Zuan Yang − *School of Chemical Engineering, Qinghai University, Xining 810016, China*

Wei Meng − *New Energy (Photovoltaic) Industry Research Center, Qinghai University, Xining 810016, China*

Lian Zhou − *New Energy (Photovoltaic) Industry Research Center, Qinghai University, Xining 810016, China*

Chunyan Sun − *School of Chemical Engineering, Qinghai University, Xining 810016, China*

Wanqin Chen − *School of Chemical Engineering, Qinghai University, Xining 810016, China*

Complete contact information is available at: https://pubs.acs.org/10.1021/acsomega.2c00476

Notes

The authors declare no competing financial interest.

■ ACKNOWLEDGMENTS

This work was financially supported by NSFC (21766028 and 21862017), The Applied Basic Research Plan of Qinghai Province (No. 2020-ZJ-722), and The Open Project of State Key Laboratory of Plateau Ecology and Agriculture, Qinghai University (No. 2019-ZZ-11). We thank Analysis Center of Qinghai University and the Modern Analysis Center of Nanjing University for samples characterization.

■ REFERENCES

(1) Wang, X. C.; Maeda, K.; Thomas, A.; Takanabe, K.; Xin, G.; Carlsson, J. M.; Domen, K.; Antonietti, M. A metal-free polymeric photocatalyst for hydrogen production from water under visible light. *Nat. Mater.* **2009**, *8*, 76−80.

(2) Stegbauer, L.; Schwinghammer, K.; Lotsch, B. V. A hydrazone-based covalent organic framework for photocatalytic hydrogen production. *Chem. Sci.* **2014**, *5*, 2789−2793.

(3) Schwab, M. G.; Hamburger, M.; Feng, X.; Shu, J.; Spiess, H. W.; Wang, X.; Antonietti, M.; Mullen, K. Photocatalytic hydrogen evolution through fully conjugated poly(azomethine) networks. *Chem. Commun.* **2010**, *46*, 8932−8934.

(4) Li, C. M.; Xu, Y.; Tu, W. G.; Chen, G.; Xu, R. Metal-free photocatalysts for various applications in energy conversion and environmental purification. *Green Chem.* **2017**, *19*, 882−899.

(5) Masih, D.; Ma, Y. Y.; Rohani, S. Graphitic C_3N_4 based noble-metal-free photocatalyst systems: A review. *Appl. Catal., B* **2017**, *206*, 556−588.

(6) Ong, W. J.; Tan, L. L.; Ng, Y. H.; Yong, S. T.; Chai, S. P. Graphitic carbon nitride (g-C_3N_4)-based photocatalysts for artificial photosynthesis and environmental remediation: Are we a step closer to achieving sustainability? *Chem. Rev.* **2016**, *116*, 7159−7329.

(7) Wang, X. C.; Blechert, S.; Antonietti, M. Polymeric graphitic carbon nitride for heterogeneous photocatalysis. *ACS Catal.* **2012**, *2*, 1596−1606.

(8) Wang, Y. Q.; Shen, S. H. Progress and prospects of non-metal doped graphitic carbon nitride for improved photocatalytic performances. *Acta Phys. -Chim. Sin.* **2020**, *36*, 1905080.

(9) Chu, S.; Wang, Y.; Guo, Y.; Zhou, P.; Yu, H.; Luo, L. L.; Kong, F.; Zou, Z. G. Facile green synthesis of crystalline polyimide photocatalyst for hydrogen generation from water. *J. Mater. Chem.* **2012**, *22*, 15519−15521.

(10) Wan, S.; Gandara, F.; Asano, A.; Furukawa, H.; Saeki, A.; Dey, S. K.; Liao, L.; Ambrogio, M. W.; Botros, Y. Y.; Duan, X. F.; Seki, S.; Stoddart, J. F.; Yaghi, O. M. Covalent organic frameworks with high charge carrier mobility. *Chem. Mater.* **2011**, *23*, 4094−4097.

(11) Dasgupta, J.; Sikder, J.; Chakraborty, S.; Adhikari, U.; Reddy, V. P.; Mondal, B. A.; Curcio, S. Microwave-assisted modified polyimide synthesis: A facile route to the enhancement of visible-light-induced photocatalytic performance for dye degradation. *ACS Sustain. Chem. Eng.* **2017**, *5*, 6817−6826.

(12) Ma, C. H.; Zhou, J.; Zhu, H. Y.; Yang, W. W.; Liu, J. G.; Wang, Y.; Zou, Z. G. Constructing a high-efficiency MoO_3/Polyimide hybrid photocatalyst based on strong interfacial interaction. *ACS Appl. Mater. Interface.* **2015**, *7*, 14628−14637.

(13) Ma, C. H.; Zhou, J.; Cui, Z. W.; Wang, Y.; Zou, Z. G. In situ growth MoO_3 nanoflake on conjugated polymer: An advanced photocatalyst for hydrogen evolution from water solution under solar light. *Sol. Energy Mater. Sol. Cells.* **2016**, *150*, 102−111.

(14) Li, J. Y.; Jiang, X.; Lin, L.; Zhou, J. J.; Xu, G. S.; Yuan, Y. P. Improving the photocatalytic performance of polyimide by constructing an inorganic-organic hybrid ZnO-polyimide core-shell structure. *J. Mol. Catal. A Chem.* **2015**, *406*, 46−50.
(15) Lin, L.; Ye, P.; Cao, C.; Jin, Q.; Xu, G. S.; Shen, Y. H.; Yuan, Y. P. Rapid microwave-assisted green production of a crystalline polyimide for enhanced visible-light-induced photocatalytic hydrogen production. *J. Mater. Chem. A* **2015**, *3*, 10205−10208.
(16) Ma, C. H.; Zhu, H. Y.; Zhou, J.; Cui, Z. W.; Liu, T.; Wang, Y. C.; Wang, Y.; Zou, Z. G. Confinement effect of monolayer MoS_2 quantum dots on conjugated polyimide and promotion of solar-driven photocatalytic hydrogen generation. *Dalton Trans.* **2017**, *46*, 3877−3886.
(17) Chu, S.; Wang, Y.; Wang, C. C.; Yang, J. C.; Zou, Z. G. Bandgap modulation of polyimide photocatalyst for optimum H_2 production activity under visible light irradiation. *Int. J. Hydrog. Energy.* **2013**, *38*, 10768−10772.
(18) Wang, C. C.; Guo, Y.; Yang, Y.; Chu, S.; Zhou, C. K.; Wang, Y.; Zou, Z. G. Sulfur-doped polyimide photocatalyst with enhanced photocatalytic activity under visible light irradiation. *ACS Appl. Mater. Interface.* **2014**, *6*, 4321−4328.
(19) Yang, S. B.; Gong, Y. J.; Zhang, J. S.; Zhan, L.; Ma, L. L.; Fang, Z. H.; Vajtai, R.; Wang, X. C.; Ajayan, P. M. Exfoliated graphitic carbon nitride nanosheets as efficient catalysts for hydrogen evolution under visible light. *Adv. Mater.* **2013**, *25*, 2452−2456.
(20) Lu, Q. P.; Yu, Y. F.; Ma, Q. L.; Chen, B.; Zhang, H. 2D transition-metal-dichalcogenide-nanosheet-based composites for photocatalytic and electrocatalytic hydrogen evolution reactions. *Adv. Mater.* **2016**, *28*, 1917.
(21) Zhou, Y. G.; Zhang, Y. F.; Lin, M. S.; Long, J. L.; Zhang, Z. Z.; Lin, H. X.; Wu, J. C. S.; Wang, X. X. Monolayered Bi_2WO_6 nanosheets mimicking heterojunction interface with open surfaces for photocatalysis. *Nat. Commun.* **2015**, *6*, 8340.
(22) Sang, Y. H.; Zhao, Z. H.; Zhao, M. W.; Hao, P.; Leng, Y. H.; Liu, H. From UV to near-infrared, WS_2 nanosheet: A novel photocatalyst for full solar Light spectrum photodegradation. *Adv. Mater.* **2015**, *27*, 363−369.
(23) Li, H. J.; Tu, W. G.; Zhou, Y.; Zou, Z. G. Z-scheme photocatalytic systems for promoting photocatalytic performance: Recent progress and future challenges. *Adv. Sci.* **2016**, *3*, 1500389.
(24) Wang, B.; Zhao, J. Z.; Chen, H. L.; Weng, Y. X.; Tang, H.; Chen, Z. R.; Zhu, W. S.; She, Y. B.; Xia, J. X.; Li, H. M. Unique Z-scheme carbonized polymer dots/$Bi_4O_5Br_2$ hybrids for efficiently boosting photocatalytic CO_2 reduction. *Appl. Catal., B* **2021**, *293*, 120182.
(25) Zhao, J. Z.; Ji, M. X.; Di, J.; Zhang, Y.; He, M. Q.; Li, H. M.; Xia, J. X. Novel Z-scheme heterogeneous photo-fenton-like g-C_3N_4/FeOCl for the pollutants degradation under visible light irradiation. *J. Photoch. Photobio. A* **2020**, *391*, 112343.
(26) Ben, H. J.; Liu, Y.; Liu, X.; Liu, X. F.; Ling, C. C.; Liang, C.; Zhang, L. Z. Diffusion-controlled Z-scheme-steered charge separation across PDI/BiOI heterointerface for ultraviolet, visible, and infrared light-driven photocatalysis. *Adv. Funct. Mater.* **2021**, *31*, 2102315.
(27) Zhang, M.; Lu, M.; Lang, Z. L.; Liu, J.; Liu, M.; Chang, J. N.; Li, L. Y.; Shang, L. J.; Wang, M.; Li, S. L.; Lan, Y. Q. Semiconductor/covalent-organic-framework Z-scheme heterojunctions for artificial photosynthesis. *Angew. Chem., Int. Ed.* **2020**, *59*, 6500−6506.
(28) Zhu, J. X.; Yin, Z. Y.; Yang, D.; Sun, T.; Yu, H.; Hoster, H. E.; Hng, H. H.; Zhang, H.; Yan, Q. Y. Hierarchical hollow spheres composed of ultrathin Fe_2O_3 nanosheets for lithium storage and photocatalytic water oxidation. *Energy Environ. Sci.* **2013**, *6*, 987−993.
(29) She, X. J.; Wu, J. J.; Xu, H.; Zhong, J.; Wang, Y.; Song, Y. H.; Nie, K. Q.; Liu, Y.; Yang, Y. C.; Rodrigues, M. T. F.; Vajtai, R.; Lou, J.; Du, D. L.; Li, H. M.; Ajayan, P. M. High efficiency photocatalytic water splitting using 2D α-Fe_2O_3/g-C_3N_4 Z-scheme catalysts. *Adv. Energy Mater.* **2017**, *7*, 1700025.
(30) Gu, H. Y.; Liu, X.; Liu, X. F.; Ling, C. C.; Wei, K.; Zhan, G. M.; Guo, Y. B.; Zhang, L. Z. Adjacent single-atom irons boosting molecular oxygen activation on MnO_2. *Nat. Commun.* **2021**, *12*, 5422.
(31) Jin, Y. X.; Tang, J.; Hu, J.; Han, X.; Shang, Y. Z.; Liu, H. L. One-step fabrication of ultralow dielectric polyimide films consisting of size-controlled mesoporous nanoparticles. *Colloids Surf., A* **2011**, *392*, 178−186.
(32) Ma, W. S.; Zeng, X. R.; Gong, K. C. Characterization of polyaniline/thiokol rubber composite films (I). *Huanan Ligong Daxue Xuebao, Ziran Kexueban* **1999**, *27*, 12−17.
(33) Fu, J.; Chang, B. B.; Tian, Y. L.; Xi, F. N.; Dong, X. P. Novel C_3N_4-CdS composite photocatalysts with organic-inorganic heterojunctions: in situ synthesis, exceptional activity, high stability and photocatalytic mechanism. *J. Mater. Chem. A* **2013**, *1*, 3083−3090.
(34) Hu, Y.; Hao, X. Q.; Cui, Z. W.; Zhou, J.; Chu, S. Q.; Wang, Y.; Zou, Z. G. Enhanced photocarrier separation in conjugated polymer engineered CdS for direct Z-scheme photocatalytic hydrogen evolution. *Appl. Catal., B* **2020**, *260*, 118131.
(35) Luo, Y. S.; Luo, J. S.; Jiang, J.; Zhou, W. W.; Yang, H. P.; Qi, X. Y.; Zhang, H.; Fan, H. J.; Yu, D. Y. W.; Li, C. M.; Yu, T. Seed-assisted synthesis of highly ordered TiO_2@α-Fe_2O_3 core/shell arrays on carbon textiles for lithium-ion battery applications. *Energy Environ. Sci.* **2012**, *5*, 6559.
(36) Li, C. M.; Du, Y. H.; Wang, D. P.; Yin, S. M.; Tu, W. G.; Chen, Z.; Kraft, M.; Chen, G.; Xu, R. Unique P-Co-N surface bonding states constructed on g-C_3N_4 nanosheets for drastically enhanced photocatalytic activity of H_2 evolution. *Adv. Funct. Mater.* **2017**, *27*, 1604328.
(37) Thangavel, N.; Bellamkonda, S.; Arulraj, A. D.; Rao, G. R.; Neppolian, B. visible light induced efficient hydrogen production through semiconductor-conductor-semiconductor (S-C-S) interfaces formed between g-C_3N_4 and rGO/Fe_2O_3 core-shell composites. *Catal. Sci. Technol.* **2018**, *8*, 5081−5090.
(38) Meng, P. C.; Heng, H. M.; Sun, Y. H.; Huang, J. H.; Yang, J. P.; Liu, X. Positive effects of phosphotungstic acid on the in-situ solid-state polymerization and visible light photocatalytic activity of polyimide-based photocatalyst. *Appl. Catal., B* **2018**, *226*, 487−498.
(39) Zhang, J. S.; Zhang, G. G.; Chen, X. F.; Lin, S.; Möhlmann, L.; Dolřga, G.; Lipner, G.; Antonietti, M.; Blechert, S.; Wang, X. C. Co-monomer control of carbon nitride semiconductors to optimize hydrogen evolution with visible light. *Angew. Chem., Int. Ed.* **2012**, *51*, 3183−3187.
(40) Kisch, H. Semiconductor photocatalysis-mechanistic and synthetic aspects. *Angew. Chem., Int. Ed.* **2013**, *52*, 812−847.
(41) Jia, X.; Tahir, M.; Pan, L.; Huang, Z. F.; Zhang, X. W.; Wang, L.; Zou, J. J. Direct Z-scheme composite of CdS and oxygen-defected $CdWO_4$: An efficient visible-light-driven photocatalyst for hydrogen evolution. *Appl. Catal., B* **2016**, *198*, 154−161.
(42) Liang, Z. Z.; Shen, R. C.; Ng, Y. H.; Zhang, P.; Xiang, Q. J.; Li, X. A review on 2D MoS_2 cocatalysts in photocatalytic H_2 production. *J. Mater. Sci. Technol.* **2020**, *56*, 89−121.
(43) Yu, G. Y.; Hu, F. X.; Cheng, W. W.; Han, Z. T.; Liu, C.; Dai, Y. ZnCuAl-LDH/Bi_2 MoO_6 nanocomposites with improved visible light-driven photocatalytic degradation. *Acta Phys. -Chim. Sin.* **2020**, *36*, 1911016.
(44) Wei, Z. D.; Xu, M. Q.; Liu, J. Y.; Guo, W. Q.; Jiang, Z.; Shangguan, W. F. Simultaneous visible-light-induced hydrogen production enhancement and antibiotic wastewater degradation using MoS_2 @$Zn_xCd_{1-x}S$: Solid-solution-assisted photocatalysis. *Chinese. J. Catal.* **2020**, *41*, 103−113.
(45) Cao, D. P.; Zhang, J. B.; Wang, A. C.; Yu, X. H.; Mi, B. X. Fabrication of Cr-doped $SrTiO_3$/Ti-doped α-Fe_2O_3 photoanodes with enhanced photoelectrochemical properties. *J. Mater. Sci. Technol.* **2020**, *56*, 189−195.
(46) Shen, R.; He, K.; Zhang, A.; Li, N.; Ng, Y. H.; Zhang, P.; Hu, J.; Li, X. In-situ construction of metallic Ni_3 C@Ni core-shell cocatalysts over g-C_3N_4 nanosheets for shell-thickness-dependent photocatalytic H_2 production. *Appl. Catal., B* **2021**, *291*, 120104.
(47) Monga, D.; Basu, S. Enhanced photocatalytic degradation of industrial dye by g-C_3N_4/TiO_2 nanocomposite: role of shape of TiO_2. *Adv. Powder Technol.* **2019**, *30*, 1089−1098.

https://doi.org/10.1021/acsomega.2c00476
ACS Omega 2022, 7, 11371−11381

(48) Zhou, X. S.; Jin, B.; Chen, R. Q.; Peng, F.; Fang, Y. P. Synthesis of porous Fe_3O_4/g-C_3N_4 nanospheres as highly efficient and recyclable photocatalysts. *Mater. Res. Bull.* **2013**, *48*, 1447−1452.
(49) Liang, R. W.; Liang, Z. Y.; Chen, F.; Xie, D. H.; Wu, Y. L.; Wang, X. X.; Yan, G. Y.; Wu, L. Sodium dodecyl sulfate-decorated MOF-derived porous Fe_2O_3 nanoparticles: High performance, recyclable photocatalysts for fuel denitrification. *Chinese. J. Catal.* **2020**, *41*, 188−199.
(50) Xu, D. F.; Cheng, B.; Cao, S. W.; Yu, J. G. Enhanced photocatalytic activity and stability of Z-scheme Ag_2CrO_4-GO composite photocatalysts for organic pollutant degradation. *Appl. Catal., B* **2015**, *164*, 380−388.
(51) He, R. A.; Chen, R.; Luo, J. H.; Zhang, S. Y.; Xu, D. F. Fabrication of graphene quantum dots modified BiOI/PAN flexible fiber with enhanced photocatalytic activity. *Acta Phys. -Chim. Sin.* **2020**, *37*, 2011022.
(52) Fang, M.-M.; Shao, J.-X.; Huang, X.-G.; Wang, J.-Y.; Chen, W. Direct Z-scheme $CdFe_2O_4$/g-C_3N_4 hybrid photocatalysts for highly efficient ceftiofur sodium photodegradation. *J. Mater. Sci. Technol.* **2020**, *56*, 133−142.
(53) Ge, S. X.; Zhang, L. Z. Efficient visible light driven photocatalytic removal of RhB and NO with low temperature synthesized In(OH)xSy hollow nanocubes: A comparative study. *Environ. Sci. Technol.* **2011**, *45*, 3027−3033.
(54) Bai, J. X.; Shen, R. C.; Chen, W. L.; Xie, J.; Zhang, P.; Jiang, Z. M.; Li, X. Enhanced photocatalytic H_2 evolution based on a Ti_3 C_2/$Zn_{0.7}Cd_{0.3}S$/Fe_2O_3 Ohmic/S-scheme hybrid heterojunction with cascade 2D coupling interfaces. *Chem. Eng. J.* **2022**, *429*, 132587.
(55) Wang, H. J.; Li, X.; Zhao, X. X.; Li, C. Y.; Song, X. H.; Zhang, P.; Huo, P. W.; Li, X. A review on heterogeneous photocatalysis for environmental remediation: From semiconductors to modification strategies. *Chinese. J. Catal.* **2022**, *43*, 178−214.
(56) Wageh, S.; Al-Ghamdi, A. A.; Jafer, R.; Li, X.; Zhang, P. A new heterojunction in photocatalysis: S-scheme heterojunction. *Chinese. J. Catal.* **2021**, *42*, 667−669.
(57) Shen, R. C.; Zhang, L. P.; Chen, X. Z.; Jaroniec, M.; Li, N.; Li, X. Integrating 2D/2D CdS/α-Fe_2O_3 ultrathin bilayer Z-scheme heterojunction with metallic β-NiS nanosheet-based ohmic-junction for efficient photocatalytic H_2 evolution. *Appl. Catal., B* **2020**, *266*, 118619.
(58) Bie, C. B.; Yu, H. G.; Cheng, B.; Ho, W. K.; Fan, J. J.; Yu, J. G. Design, fabrication, and mechanism of nitrogen-doped graphene-based photocatalyst. *Adv. Mater.* **2021**, *33*, 2003521.
(59) Wang, Y. M.; Zhang, S. P.; Ge, Yu; Wang, C. H.; Hu, J.; Liu, H. L. Highly efficient photocatalytic degradation of tetracycline using a bimetallic oxide/carbon photocatalyst. *Acta Phys. -Chim. Sin.* **2020**, *36*, 1905083.
(60) Li, S. J.; Wang, C. C.; Cai, M. J.; Yang, F.; Liu, Y. P.; Chen, J. L.; Zhang, P.; Li, X.; Chen, X. B. Facile fabrication of TaON/Bi_2MoO_6 core-shell S-scheme heterojunction nanofibers for boosting visible-light catalytic levofloxacin degradation and Cr(VI) reduction. *Chem. Eng. J.* **2022**, *428*, 131158.
(61) Wang, W. L.; Zhao, W. L.; Zhang, H. C.; Dou, X. C.; Shi, H. F. 2D/2D step-scheme α-Fe_2O_3/Bi_2WO_6 photocatalyst with efficient charge transfer for enhanced photo-Fenton catalytic activity. *Chinese. J. Catal.* **2021**, *42*, 97−106.

https://doi.org/10.1021/acsomega.2c00476
ACS Omega 2022, 7, 11371−11381